ACS APPLIED NANO MATERIALS

www.acsanm.org Article

Conformation Regulation of $Ti_3C_2T_x$ MXene via Interfacial Energy for Tunable Strain-Sensing Behaviors

Hao Ouyang,‡ Hao Tang,‡ Liangjing Shi, Evgeniya Sheremet, Raul D. Rodriguez, Jing Sun, Yin Cheng,* and Ranran Wang*

Cite This: *ACS Appl. Nano Mater.* 2026, 9, 5132−5143 Read Online

ACCESS | Metrics & More | Article Recommendations | Supporting Information

ABSTRACT: The processing of two-dimensional transition-metal carbides or nitrides (MXenes) has boosted their applications in numerous technological fields, ranging from energy storage to electromagnetic shielding and flexible sensing devices. The microstructure design of MXene films is key to the mechano-responsive performance. Here, we propose a simple and efficient method to modulate the microstructure of the MXene film via different solvents. MXene films with microstructures ranging from flat stacking, warping, and crumpling to folding tubes and cages are obtained through tuning the Hansen solubility parameters of the solvents, giving rise to distinctive strain-sensing behaviors. The MXene devices obtained from nonpolar solvents demonstrate an anomalous negative resistance−strain response, which was illustrated by a compression-crack synergetic sensing mechanism. Such strain sensors can generate distinct waveforms across varying amplitudes in response to the same movement rather than merely exhibiting amplitude differences. This enhances the specificity of strain recognition, offering the potential for precise motion identification and standardized movement training.

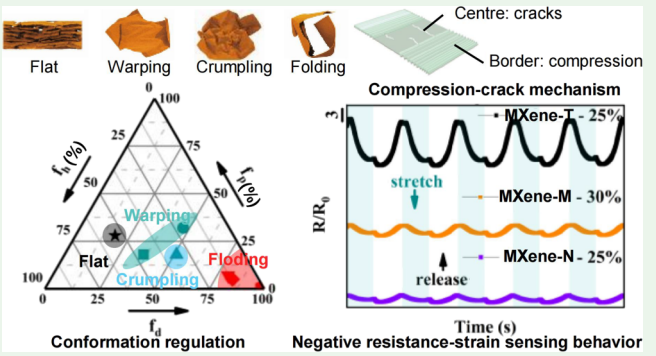

KEYWORDS: *MXenes, microstructure regulation, strain sensor, wearable electronics, motion recognition*

INTRODUCTION

As a novel class of two-dimensional macromolecules, MXenes have many desirable characteristics, including metal-like conductivity, large specific surface area, good hydrophilicity, and flexibility,[1−4] which makes them promising in the application of electromagnetic shielding,[5−8] supercapacitors,[9−11] lithium-ion batteries,[12−15] and flexible sensors.[16−19] In addition to the intrinsic properties, microstructure conformations and stacking structures of MXenes also influence the performance of the assemblies. For example, asymmetric interlayer distance led to excellent actuating response of $Ti_3C_2T_x$ MXene films to sunlight;[20] Ti_3CNT_x MXene with a layered, metamaterial-like structure exhibited an anomalously high absorption of electromagnetic waves;[5] MXene nanocomposite-based strain sensors with tile-like stacked hierarchical microstructures showed high sensitivity and wide detection range.[21] Therefore, developing facile methods to regulate the conformation and stacking structure of MXenes is of great significance for extended applications and optimized performance.

Recent advances in wearable conductive systems have mainly focused on supramolecularly engineered polymer hydrogels, ultrathin ionic electrodes, and soft bioelectronic interfaces to enhance mechanical compliance and signal stability.[22−24] These strategies predominantly optimize polymer−network interactions and ionic conduction pathways. In contrast, the intrinsic conformational topology of two-dimensional conductive building blocks has rarely been explored as a programmable parameter for electromechanical regulation. Here, we propose a solvent-mediated strategy to modulate the MXene stack conformation, enabling polarity-dependent strain response and activation-tunable sensing behavior.

While previous strategies predominantly optimize stacking order and interlayer alignment via solvent permittivity[25] or tailor the transport channels within lamellar membranes for molecular separation,[26] or even utilize physical templates such as controlled freezing to regulate stacking and delamination,[27] the regulation of nanosheet conformation, i.e., the transition from 2D flat sheets to 3D high-energy geometries, remains an unexplored dimension for electromechanical modulation. More importantly, how such conformational transitions alter percolation topology and strain response mechanisms has not been systematically investigated. Diverse conformational

Received: December 31, 2025
Revised: February 26, 2026
Accepted: March 3, 2026
Published: March 11, 2026

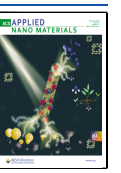

https://doi.org/10.1021/acsanm.5c05888
ACS Appl. Nano Mater. 2026, 9, 5132−5143

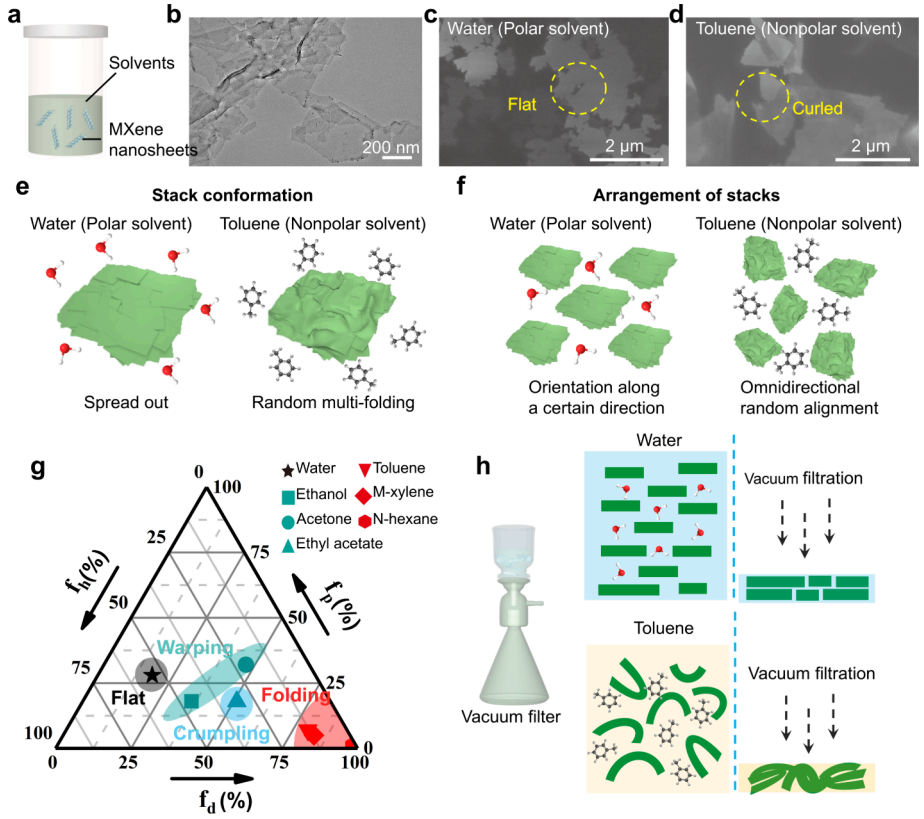

Figure 1. (a) Dispersion of $Ti_3C_2T_x$ MXene nanosheets in different solvents; (b) the TEM image of $Ti_3C_2T_x$ MXene nanosheets (lateral dimensions: 100−400 nm); the SEM image of MXene stacks dispersed in liquid (c) water and (d) the toluene environment; (e) the schematic diagram of MXene stack conformation dispersed in polar and nonpolar solvent environments (not to scale); (f) the schematic diagram of the arrangement of MXene stacks in polar and nonpolar environments (not to scale); (g) distribution of seven selected solvents in the Teas triangle graph (green: polar solvent, red: nonpolar solvent), f_d, f_p, and f_h denote the dispersion fractional parameter, the polar fractional parameter, and the hydrogen bonding fractional parameter, respectively; (h) vacuum filter for solute−solvent separation and vacuum filtration process of MXene stacks in water or toluene dispersion (not to scale).

phases of 2D molecules have been predicted in theory, but only a few of them have been experimentally verified. In a recent study, Wang established the conformational phase map of 2D molecules in solution using single-layer graphene oxide as the experimental model, thereby providing guidance for manipulating the conformations of 2D materials.[28] Unlike graphene oxide, MXene consists of multilayered atomic structures and abundant functional groups (−O, −OH, and −F). These surface terminations significantly dictate the surface energy and interlayer environment, adding to the complexity of predicting its conformational behavior.[29,30] MXenes with conformations beyond a flat structure have been shown in several pioneering works. Vaughn fabricated Ti_2C MXene of plates, crumpled sheets, spheres, and scrolls through selective intercalation of *p*-phosphonic calix[*n*] arenes (PCX*n*, *n* = 4, 5, 6, or 8).[31] However, the underlying mechanism of the conformation regulation and the influence of PCX*n* on the properties of MXene stay obscure. Zhao used alkali metal ions to induce fluctuations in MXene lamellae yielding crumpled MXene nanosheets, which displayed high capacity and outstanding rate performance as anode materials for sodium ion batteries.[32] Despite the existence of a few reported property control pathways, a versatile approach to easily maneuver the conformations of MXene targeting the modulation of strain-sensing behavior is still lacking.

Herein, we propose a novel method to regulate the conformations of MXene lamellae. By dispersing $Ti_3C_2T_x$ MXene in different solvents, conformation variations, including stacking flat, warping, crumpling, folding tubes, and cages, are obtained. MXene films made from these solutions preserved the original conformations of $Ti_3C_2T_x$ MXene and showed distinct strain-sensing behaviors. A positive strain gauge factor was observed from MXene film strain sensors prepared by using polar solvents (MXene-polar solvent sensors), while a negative strain gauge factor occurred in the MXene-nonpolar solvent sensors. The compression-crack synergetic mechanism was proposed for the first time to unravel the unique strain-sensing behavior. Moreover, the strain-sensing performance of the MXene-nonpolar solvent devices can be modulated by the very initial strain, which endows the devices with the potential for personalized customization.

RESULTS AND DISCUSSION

Conformation Regulations of $Ti_3C_2T_x$ MXene

Delaminated $Ti_3C_2T_x$ MXene nanosheets were synthesized by etching Ti_3AlC_2 with a mixture of lithium fluoride (LiF) and hydrochloric acid (HCl), which was confirmed by the shift of the (002) peak to a low angle and the disappearance of the (104) peak in XRD patterns (Figure S1). As shown in Figure 1a, delaminated $Ti_3C_2T_x$ MXene nanosheets in seven different solvents, including water, ethanol, acetone, ethyl acetate, toluene, *m*-xylene, and *n*-hexane, were obtained through ultrasonic dispersion. The transmission electron microscope

https://doi.org/10.1021/acsanm.5c05888
ACS Appl. Nano Mater. 2026, 9, 5132−5143

(TEM) image in Figure 1b indicates that the size distribution of these nanosheets ranges from 100 to 400 nm. The samples dispersed in two representative solvents (polar solvent: water; nonpolar solvent: toluene) were characterized by scanning electron microscopy (SEM) as shown in Figure 1c (water) and Figure 1d (toluene). In both solvents, the nanosheets are stacked with each other, forming larger MXene stacks at the micron scale. The $Ti_3C_2T_x$ MXene stacks dispersed in water are flat and oriented along a certain direction, while those dispersed in toluene are folded randomly and arranged in all directions.

The stack conformation variation (Figure 1e) is mainly attributed to the disproportional affinity of $Ti_3C_2T_x$ MXene to different solvents. Here, conformation refers to the stacking architecture of multilayer MXene domains rather than large-scale mechanical bending of isolated monolayer nanosheets. Many hydrophilic terminations, such as hydroxyl groups, exist on the surface of $Ti_3C_2T_x$ MXene nanosheets, which endow them with high affinity to water while having high mutual repulsion to toluene. The strong surface energy mismatch leads to random multifolding of $Ti_3C_2T_x$ MXene stacks in toluene.

As for the arrangement of MXene stacks (Figure 1f), it mainly depends on the van der Waals force between the $Ti_3C_2T_x$ MXene and solvent molecules. The −OH, −O, and −F terminations, owing to their high electronegativity, cause the electron cloud to shift toward the surface and separate the positive and negative charge centers. This creates an inherent dipole moment in $Ti_3C_2T_x$ MXene stacks, endowing them with polarity. Therefore, an orientation force occurs between these stacks and the polar solvent molecules. Dipoles with opposite orientations repel each other, while similarly oriented dipoles attract. As a result, both the MXene sheet and solvent molecules are bound to rotate relative to each other, which explains the flat dispersion seen when $Ti_3C_2T_x$ MXene stacks along a certain direction. The above situation is notable in an aqueous environment with high polarity, while in nonpolar solvents like toluene, solvent molecules form dipoles solely through the polar induction of MXene stacks, resulting in significantly weaker orientation forces. Therefore, MXene stacks exhibit omnidirectional alignment in toluene.

Based on the above observations of $Ti_3C_2T_x$ MXene nanosheets in water or toluene, it can be concluded that their dispersion state in different solvents is closely related to the degree of interaction with solvent molecules. Therefore, we introduce Hansen solubility parameters as semiquantitative descriptors to rationalize differences in solvent−MXene interaction compatibility. Cohesive energy density is a physical parameter that directly reflects the ability of solvent molecules to interact with each other, and its square root is defined as the Hildebrand solubility parameter, which is indicated by the following formula,

$$\delta = \sqrt{\frac{\Delta H - RT}{V_m}}$$

where δ, ΔH, R, T, and V_m represent the solubility, heat of vaporization, gas constant, temperature, and molar volume, respectively.[33] However, the Hildebrand solubility parameter reflects the sum of all intermolecular interactions, and solvents with the same value may show different solubilities for the same substance. The Hildebrand solubility parameter quantifies the sum of all intermolecular interactions, but solvents with identical δ values may exhibit different solubilities for the same substance as existing differences in the nature and contribution of their individual intermolecular forces. Thus, the Hildebrand solubility parameter is further divided into three parts in Hansen components parameters, and the conversion formula of which is as follows

$$\delta_t^{\,2} = \delta_d^{\,2} + \delta_p^{\,2} + \delta_h^{\,2}$$

where δ_t is the total Hildebrand parameter, and the three parts include dispersion component parameter, polar component parameter, and hydrogen bonding component parameter. Converting Hansen component parameters to a fractional form provides a more intuitive representation of the relative contributions of each component.

$$f_d = \frac{\delta_d}{\delta_d + \delta_p + \delta_h} f_p = \frac{\delta_p}{\delta_d + \delta_p + \delta_h} f_h = \frac{\delta_h}{\delta_d + \delta_p + \delta_h}$$

where a larger value in f_d indicates that the dispersion component dominates the cohesive energy density, corresponding to a more nonpolar solvent character. To exhibit the component parameters of various solvents more directly, the fractional parameters are marked in the Teas triangle graph (Figure 1g, Table S1). In addition to water and toluene, five other solvents were also used to disperse the $Ti_3C_2T_x$ MXene nanosheets. Water, ethanol, acetone, and ethyl acetate are classified as polar solvents ($f_d \lesssim 50\%$) and are listed here in order of decreasing polarity. Toluene, m-xylene, and *n*-hexane are nonpolar solvents ($f_d > 50\%$), in which the polar components of the first two are similar, while *n*-hexane only contains the dispersion component. It should be noted that Hansen solubility parameters (HSPs) are employed here as compatibility descriptors rather than strict interfacial energy measurements. While HSPs are bulk thermodynamic descriptors, they serve as compatibility descriptors correlated with solvent-surface affinity between solvents and 2D nanosheets, as the enthalpy of mixing is minimized when their values are matched. This framework treats the heterogeneous $Ti_3C_2T_x$ surface (−O, −OH, and −F) as a composite interface, where the tripartite HSP values capture the cumulative interactions of these functional sites, an approach supported by recent studies on the swelling behavior and chemical activity of MXene surface groups.[29,30] Accordingly, the distribution of solvents in the Teas triangle reflects correlation trends in solvent−MXene interactions rather than a sharp thermodynamic phase boundary. Direct interfacial measurements (e.g., contact angle) probe partially wetted film surfaces, whereas the conformational regulation process occurs in fully solvated dispersion states. Instead, dispersion-based tests provide a holistic view of the interaction in a fully wetted state, which is more representative of the spontaneous conformation regulation process.

As outlined above, we aim to modulate the conformations of the MXene stacks by using solvents with different polarities. For preserving the different conformations of $Ti_3C_2T_x$ MXene stacks and assembling them into conductive networks, vacuum filtration was employed to realize rapid solvent−solute separation and to prepare $Ti_3C_2T_x$ MXene films (Figure 1h). In our concept, the MXene stacks dispersed in water are suspended parallel to the liquid surface, and they are assembled into a compact film with layered structure after vacuum filtration, as described in most papers;[7,34−36] as for the toluene dispersion system, the randomly multifolded and omnidirectional randomly arranged MXene stacks result in the

https://doi.org/10.1021/acsanm.5c05888
ACS Appl. Nano Mater. 2026, 9, 5132−5143

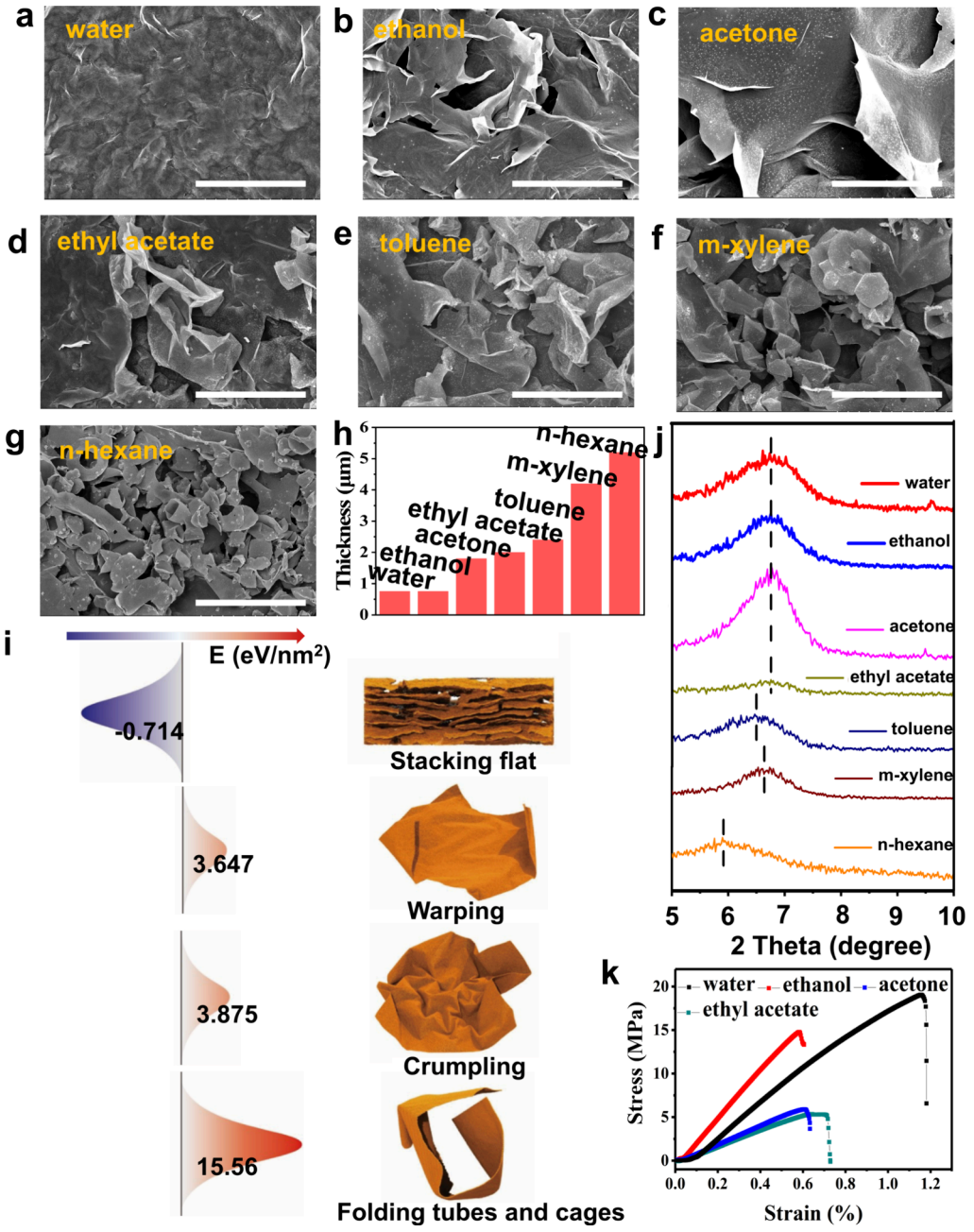

Figure 2. Top-view SEM images of $Ti_3C_2T_x$ MXene films prepared with (a) water, (b) ethanol, (c) acetone, (d) ethyl acetate, (e) toluene, (f) *m*-xylene, and (g) *n*-hexane dispersions. The scale bar is 5 μm; (h) the thickness of $Ti_3C_2T_x$ MXene films prepared with seven solvents using the same amount of nanosheets. See Figure S2 for the cross-sectional SEM images; (i) illustration of conformation and potential energy landscape of the $Ti_3C_2T_x$ MXene stack; (j) the (002) peak position in the XRD pattern of $Ti_3C_2T_x$ MXene films prepared with various solvents; (k) the stress–strain curves of $Ti_3C_2T_x$ MXene films prepared with polar solvents.

corresponding film with smaller bulk density and larger porosity, while solvents with polarity between the two extremes can be employed to regulate and achieve structures intermediate between them. Controlling the structure of conductive films enables control over their mechanical and electrical properties.

Microstructures of $Ti_3C_2T_x$ MXene Films Regulated by Solvent

The surface microstructures of $Ti_3C_2T_x$ MXene films prepared with seven solvents were characterized by SEM and are shown in Figure 2a–g. Intuitively, the MXene film prepared from MXene-water dispersion (MXene-W film, Figure 2a) was composed of lots of parallel stacked MXene sheets (Figure S2), and there were many wrinkles on the surface of the film, which is similar to the previously published results.[37] In the films prepared with the other three polar solvents with gradually reduced polarity (Figure 2b–d), it can be clearly seen that the edge warping and crumpling of MXene stacks occurs in turn. The random multifolding phenomenon can be clearly seen in the films prepared by the three nonpolar solvents (Figure 2e–g) and becomes more obvious with the increase of dispersion component parameter of the solvent (less polar).

Moreover, the arrangement of MXene stacks is also gradually changing. The transition of MXene stacks from

https://doi.org/10.1021/acsanm.5c05888
ACS Appl. Nano Mater. 2026, 9, 5132–5143

parallel to random arrangement confirms that the weakened dipole moment of solvent molecules leads to failure of the stack orientation. Due to differences in microstructure introduced by reducing solvent polarity, the film thickness increases, and bulk density decreases gradually. For instance, using the same amount of nanosheets (~2 mg), the thickness of the MXene film prepared with toluene (MXene-T film) is ~3.2 times that of the MXene-W film (Figure 2h, Figure S2). It should be mentioned that the white particles distributed on $Ti_3C_2T_x$ MXene in SEM images are not oxidation products, but LiF cubic crystals (Figure S3), which precipitated due to the insolubility of LiF in organic solvents (LiF is slightly soluble in water, so fewer white particles were observed in the MXene-W film).

The conformational evolution described above is a compromise between the driving force originating from the solvent and the mechanical properties of $Ti_3C_2T_x$ MXene. At the nanosheet level, solvent-dependent surface interactions modify the effective conformational energy landscape of individual $Ti_3C_2T_x$ sheets, influencing their local out-of-plane undulation tendency in dispersion. These nanoscale energetic variations affect how adjacent sheets approach and assemble during solvent evaporation, thereby translating into distinct stacked architectures in the solid-state film. To further clarify the internal relationship between the polarity of the solvents and $Ti_3C_2T_x$ MXene stack conformations, a coarse-grained molecular dynamics simulation was employed to estimate the potential energy landscape of four typical conformations. As shown in Figure 2i, taking the flat mechanically flexible $Ti_3C_2T_x$ MXene nanosheet as the zero potential energy standard, it is found that MXene nanosheets stacked with each other to form a flat $Ti_3C_2T_x$ MXene stack can reduce the total potential energy, and stacking occurs spontaneously. The potential energy required for the MXene stack to adopt the other three conformations is greater than zero, which means that an additional driving force is needed to induce transformation to these conformations. Among them, the energy required for crumpling is slightly higher than that of warping, while the potential energy of tubing is the highest. The potential energy landscape of the four typical configurations obtained by simulation obviously correlates with the interfacial energy between the solvent and MXene nanosheets. The surface energy mismatch between hydrophilic terminations of MXene nanosheets and solvents drives the nanosheets to form a conformation in order to minimize the system free energy, i.e., the energy of conformation formation is covered by the interfacial energy. The greater the solvent's nonpolarity encountered by hydrophilic groups, the higher the interfacial energy becomes, leading to spontaneous formation of conformations with higher potential energy. Although the warping, crumpling, and folding conformations correspond to higher potential energy states compared with flat stacks, these conformations are preserved during solvent evaporation due to kinetic trapping. During drying, rapid solvent removal induces close interlamellar contact and network formation, which restricts large-scale sliding and structural relaxation. The energy barrier required to flatten bent or folded MXene lamellae exceeds the thermal energy available under ambient drying conditions. Consequently, the solvent-induced conformations are mechanically stabilized in the solid-state films rather than relaxing back to the flat configuration. This corresponds to the distribution of solvent Hansen solubility parameters in the Teas triangle graph (Figure 1g): The conformations corresponding to the four sets as polarity decreases (f_d increases) are flat, warping, crumpling, and folding; moreover, the proportion of folded conformation increased in turn among the MXene films prepared with toluene, *m*-xylene (MXene-M film), and *n*-hexane (MXene-N film).

To further investigate the structural variations of films prepared using seven solvents, the shift of the (002) peak position was analyzed through an X-ray diffractometer (XRD). As shown in Figure 2j, the (002) peak positions of MXene-polar solvent films are almost identical (corresponding to the interlayer spacing of 13.074 Å, Table S2), while those of the MXene-nonpolar solvent films are shifted to low angles (corresponding to larger interlayer spacing). During the dispersion process of MXene powders obtained by freeze-drying, the solvent molecules fill the spacing between nanosheets, and the intrinsic dipole moments of MXene and solvent molecules interact and reach an equilibrium. Because the dipole moment of $Ti_3C_2T_x$ MXene is fixed, the number of polar molecules that can be accommodated between nanosheets is limited by the electrostatic repulsion. In comparison, the intrinsic dipole of nonpolar solvents is much lower, resulting in a weaker built-in electric field than polar molecules, so it is easier for them to enter and obtain a larger interlayer spacing. Additionally, note that the difficulty for solvent molecules entering the interlayer is also related to the molecular volume. Specifically, toluene and *m*-xylene have similar Hansen solubility parameters, but the latter has one more methyl than the former, which makes it more difficult to enter the interlayer, resulting in the difference between the positions of the (002) peaks. In summary, the layer spacing of $Ti_3C_2T_x$ MXene nanosheets can also be regulated through solvent dispersion.

The difference in the microstructure is reflected in the mechanical properties of $Ti_3C_2T_x$ MXene films. All films were prepared from the same delaminated $Ti_3C_2T_x$ dispersion batch under identical filtration and drying conditions, ensuring a consistent flake size distribution and minimal residual solvent. Therefore, solvent variation represents the primary systematically tuned parameter in this study. To disclose this difference, free-standing films were prepared by vacuum filtering 30 mg of $Ti_3C_2T_x$ MXene nanosheets dispersed in polar solvents, and their stress−strain curves were measured accordingly. As shown in Figure 2k, the tensile strength (19.04 MPa) and fracture strain (1.15%) of the MXene-W film are the largest, and Young's modulus is calculated to be 1.65 GPa, which is slightly lower than the reported value in a previous study[38,39] due to the smaller size of $Ti_3C_2T_x$ MXene nanosheets used in this paper. The MXene films prepared with ethanol (MXene-E film) exhibit the highest Young's modulus (2.55 GPa). Thermogravimetric analysis (Figure S4) indicates that only a negligible amount of solvent residue remains between the MXene nanosheets after vacuum drying. Due to its higher boiling point, trace amounts of water may be retained more easily during drying, which slightly facilitates interlayer slip and contributes to the lower Young's modulus of the MXene-W film compared with the MXene-E film. Note that the residual solvent content is minimal, and the organic solvents used are electrically insulating; therefore, solvent residues are unlikely to contribute directly to charge transport or resistance variation.

For the films prepared with acetone (MXene-A film, 0.97 GPa) and ethyl acetate (MXene-Ea film, 0.84 GPa), the change in Young's modulus is consistent with the bulk density. With

https://doi.org/10.1021/acsanm.5c05888
ACS Appl. Nano Mater. 2026, 9, 5132−5143

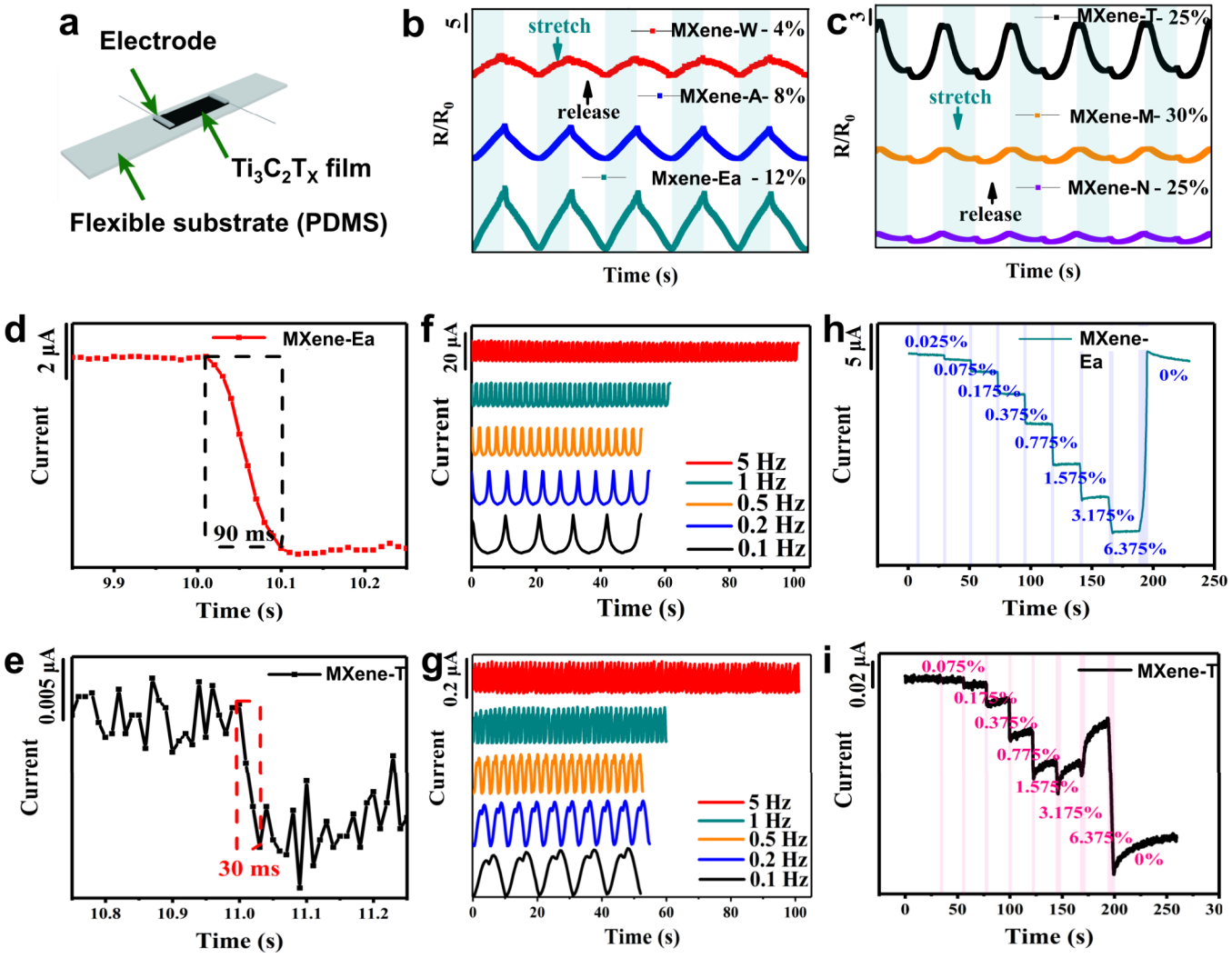

Figure 3. (a) Composition of the flexible strain sensor based on the $Ti_3C_2T_x$ MXene film; the relative resistance variation of devices prepared with (b) polar solvents and (c) nonpolar solvents under repeated stretching in selected range indicated in the legend (the shadowed parts are the stretched phases, while the blank parts correspond to the released phases); current−time curve for device prepared with (d) ethyl acetate and (e) toluene under 1% strain process (loading speed: 40 mm s^{-1}); current signal variation of the device prepared with (f) water and (g) toluene under 10% strain with different frequencies. Current variation of the device prepared with (h) ethyl acetate and (i) toluene under a step strain.

decreasing solvent polarity, the solvent-regulated stacking configuration becomes progressively less compact, accompanied by reduced bulk density and weakened effective interlayer load transfer. As a result, the measured Young's modulus decreases accordingly. Under the controlled fabrication conditions presented here, solvent polarity acts as the dominant structural modulation parameter rather than the sole intrinsic determinant of mechanical stiffness. In addition, there is a yielding phenomenon that appears in the corresponding stress−strain curve of the MXene-Ea film, originating from the slippage of the MXene stack.

Performance of Flexible Strain Sensors Based on Solvent Regulated Films

To systematically explore the strain response behavior of these $Ti_3C_2T_x$ MXene films, we took them as sensitive materials and constructed flexible strain sensors. Briefly, MXene films prepared with different solvents were transferred to the surface of an elastic poly(dimethylsiloxane) (PDMS) substrate. Electrical contacts and wires were subsequently attached to the film on both ends to measure the electrical response under the uniaxial tension (Figure 3a). The ratio of the relative resistance change to strain of the device during stretching is defined as the gauge factor (GF), which is often employed to evaluate the sensitivity of a flexible strain sensor.

$$GF = \frac{\frac{(R - R_0)}{R_0}}{\varepsilon}$$

In the formula, R and R_0 are the resistances of the device in the stretched and initial states, respectively, and ε is the corresponding strain. The relative resistance variation−strain curves for the seven $Ti_3C_2T_x$ MXene sensors prepared by using different solvents are plotted in Figure S5, and their respective sensitivities are summarized in Table S3. For 2 mg of $Ti_3C_2T_x$ MXene nanosheets, the working range of the flexible strain sensor increases gradually with the decrease of solvent polarity, while the sensitivity under the same strain decreases gradually (except for the MXene-N device). Specifically, the overall working range of MXene-polar solvent devices is below 50% strain, while that of MXene-nonpolar solvent devices can easily exceed 80% strain. This is because the gradual decrease of the

https://doi.org/10.1021/acsanm.5c05888
ACS Appl. Nano Mater. 2026, 9, 5132−5143

film's bulk density alleviates stress concentration and promotes the slippage of MXene stacks, thus inhibiting the formation of perfoliate cracks and maintaining the integrity of the conductive path.

Unexpectedly, the resistance variation trend with strain of MXene-nonpolar solvent devices displayed wide differences with that of MXene-polar solvent devices during the stretch-release cycling, although that of the seven devices presented a similar trend during the first stretching. We selected a quarter of the maximum working range of each device as the cycling condition to compare their normalized resistance (R/R_0) changes during this process. Figure 3b demonstrates the triangular change in resistance of MXene-polar solvents devices, which is consistent with the response behavior of sensors fabricated for many previously reported devices,[40−42] corresponding to the crack opening and healing in the film's structures. Meanwhile, the resistances of MXene-nonpolar solvent devices show parabolic response curves (Figure 3c), and the variation trend is opposite to that of MXene-polar solvent devices in both stretching and release stages. In other words, a positive resistance−strain response was observed from the MXene-polar solvents devices, while a negative resistive−strain response occurred in the MXene-nonpolar solvent devices. This phenomenon corresponds to a novel resistance response mechanism, which is elucidated in the following sections.

The MXene-Ea and MXene-T devices (after the first stretching) were selected as representative samples to test the sensing performance in more detail. We first investigated the appropriate content of $Ti_3C_2T_x$ MXene nanosheets to optimize the sensitivity and working range of our devices (Figure S6, 4 mg for MXene-polar solvent film; 2 mg for MXene-nonpolar solvent film) and took it as the unified standard for the following performance tests. As shown in Figure 3d,e, the response times of the two devices are 90 ms (MXene-Ea) and 30 ms (MXene-T), which are sufficient to realize the rapid sensing of strain. In addition, the real-time current curve of the MXene-T device exhibits more obvious noise due to its larger film resistance and smaller current variation. The dynamic response of the two devices to frequencies between 0.1 and 5 Hz under 10% strain exhibits a highly repeatable peak shape and amplitude (Figure 3f,g), which indicates that both sensors are capable of ensuring the authenticity of the output signal in this frequency range. Figure 3h shows the real-time current curve of the MXene-Ea device during step strain from 0.025 to 6.375% and then back to the initial state. It is concluded that this strain sensor has a detection limit of 0.025%, which fully meets the requirements for sensing small deformations, and its current variation trend is consistent with continuous stretching results. The MXene-T device also has a detection limit as low as 0.05% (Figure 3i). However, due to its unique response curve, the device's current increased during the 3.175−6.375% step strain and decreased during the 6.375−0% release stage, which is contrary to the change trend of the MXene-Ea device. Moreover, the durability of MXene-Ea and MXene-T devices was tested, and the results are shown in Figure S7. The former shows small signal degradation during 500 cycles, while the latter always maintains a consistent peak shape in a long-time test.

Compression-Crack Synergetic Sensing Mechanism

The strain-sensing behavior originates from mesoscale conductive network evolution within MXene stacks rather than reversible bending of individual $Ti_3C_2T_x$ nanosheets. To reveal the intrinsic mechanism of MXene-nonpolar solvent devices with the negative resistive−strain response, dynamic stretching *in situ* scanning electron microscopy was employed to record the microstructures of the $Ti_3C_2T_x$ MXene conductive network under different strains. As a comparison sample, Figure 4a,b and Figure S8 confirm the crack

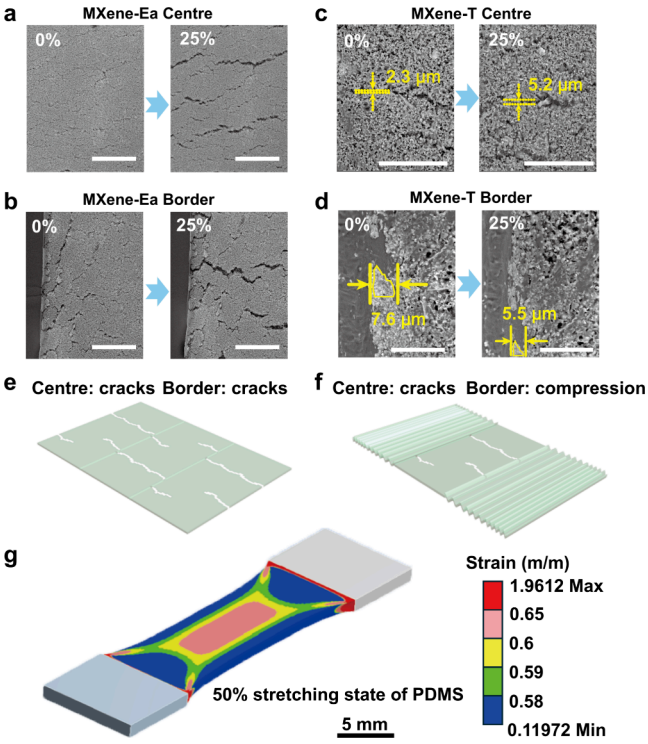

Figure 4. Dynamic stretching *in situ* SEM images of devices prepared with ethyl acetate and toluene. (a) Central area of MXene-Ea device (the scale bar is 100 μm), (b) boundary area of MXene-Ea device (the scale bar is 100 μm), (c) central area of MXene-T device (the scale bar is 50 μm), (d) boundary area of MXene-T device (the scale bar is 20 μm); the main sensing mechanism of the $Ti_3C_2T_x$ MXene conductive network prepared with (e) ethyl acetate and (f) toluene; (g) finite element simulation of the PDMS flexible substrate under 50% strain.

mechanism existing at the center and boundary of MXene-Ea conductive network, which is the working principle of most resistive strain sensors.[18,43,44] The appearance and propagation of cracks can release the stress concentration in the $Ti_3C_2T_x$ MXene conductive network. However, strain sensing based on this mechanism exhibits a trade-off between sensitivity and working range (rapid crack propagation often corresponds to higher sensitivity, but the device also loses conductivity quickly). Similar structure−property correlations have been reported in recently developed MXene and other nanomaterial-based flexible sensing systems, where microstructural regulation of conductive networks plays a decisive role in balancing electromechanical response and mechanical robustness.[45−47] Different from the MXene-Ea sample, we observed two structural changes: crack propagation in the central region and compression-assisted structural narrowing in the boundary region of the MXene-T conductive network (Figure 4c,d, and Figure S9). As shown in Figure 4d, a feature site at the boundary of the conductive network was marked, and it was found that its size perpendicular to the stretching direction

https://doi.org/10.1021/acsanm.5c05888
ACS Appl. Nano Mater. 2026, 9, 5132−5143

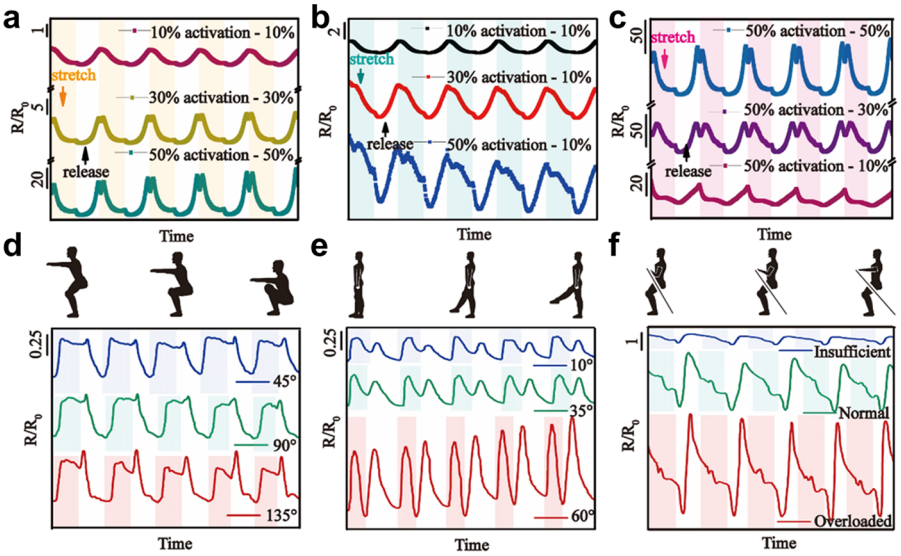

Figure 5. Signal modulation characteristics of the flexible strain sensor prepared with toluene. (a) Corresponding range stretching under different activation strains; (b) same range stretching under different activation strains; (c) different range stretching under same activation strain; detection of various physiological activities through flexible strain sensor prepared with toluene, (d) attached to the knee for repeated squats with different levels; (e) connected to the crotch for repeated goose step with different heights; (f) integrated in the elastic band for weight-bearing training with different loads.

gradually decreased with the increase of strain, indicating the narrowing of the whole structure. The in-plane compression within the low-density MXene-T conductive network facilitates partial crack closure and enhanced interflake contact, leading to a reduction in device resistance, which is completely opposite to the effect of the crack mechanism. The compression-assisted structural narrowing originates from the lateral contraction of the elastomeric substrate (positive Poisson's ratio) under tensile loading. This substrate-induced in-plane compression is mechanically transferred to the low-density MXene stack network, where it promotes crack closure and conductive pathway reconfiguration. PDMS functions only as a mechanically compliant support, while the resistance modulation arises from structural evolution within the MXene conductive network. Therefore, the inward compression deformation also exists in the MXene-polar solvent devices, but it is often released through cracks because of the films' compact microstructure.

The strain response mechanisms of MXene-Ea and MXene-T conductive networks are more intuitively compared in Figure 4e,f. For the MXene-T device, the variation in resistance under the combined action of the two mechanisms depends on which mechanism is dominant. From a percolation perspective, the total resistance can be qualitatively described as the sum of a connectivity-related component and a crack-related component. The nonlinear competition between these two contributions gives rise to the observed parabolic resistance–strain behavior. Such microstructure-governed electromechanical modulation highlights the importance of conductive network topology engineering, which has also been demonstrated as a key strategy in advanced MXene-based and quasi-homogeneous integrated sensing platforms.[47] It should be noted that the central area of the MXene-T conductive network is a complete whole before the first stretching process so that most electric charges are conducted through this area. After the first stretching, numerous cracks occur in the central area and the main conductive path is transferred to the boundary position at this time, making the effect of the compression mechanism more significant. This explains why MXene-nonpolar solvent devices exhibited distinct responses during the first and subsequent stretches, where the first cycle corresponds to network initialization and the following cycles reflect stabilized reversible electromechanical modulation. Further considering that the $Ti_3C_2T_x$ MXene conductive network is mainly affected by the deformation of the flexible substrate, we used the finite element simulation method to analyze the strain distribution in a PDMS cuboid under 50% uniaxial stretching (Figure 4g). The result suggests that the strain decreases gradually from the center to the boundary of a flexible substrate. The central area limited by the surrounding material resembles biaxial strain, while the boundary area is less affected by the transverse load and resembles uniaxial strain, which explains why the compression phenomenon at the boundary is much more obvious than that at the center. Although $Ti_3C_2T_x$ MXene on PDMS is used as a model system in this work, the compression-crack synergetic mechanism is not inherently limited to this specific material combination. The key requirements include a low-density, deformable conductive network and a flexible substrate with a positive Poisson's ratio, which suggests that this mechanism could be extended to other MXenes or layered conductive films with similar microstructural characteristics.

Modulation Characteristics of the Device and Its Application in Physiological Activity Detection

In the further study of the MXene-T device, we found its modulation characteristics; that is, the whole film spontaneously forms differentiated conductive networks after experiencing different initial strains, which also means that the sensing performance of our device can be controlled. In short, the device's performance can be customized depending on the first stretching stage, so we called it the activation stage. It should be emphasized that this activation process represents structural initialization rather than continuous damage accumulation. Before activation, the conductive network remains in a metastable stacked configuration formed during

https://doi.org/10.1021/acsanm.5c05888
ACS Appl. Nano Mater. 2026, 9, 5132−5143

solvent evaporation. The first loading cycle induces controlled microcrack nucleation and redistribution of interstack contacts, establishing a stabilized percolation topology. After this initialization, subsequent strain cycles primarily involve reversible crack opening/closing and contact density modulation within this stabilized network. This is because many irreversible cracks appeared in the central area of the conductive network during the first stretching and the state of these cracks determines the degree of influence of the cracks and the compression mechanism. The devices activated at 10, 30, and 50% strain are further cycled under their corresponding strain. Additional device-to-device measurements for independently fabricated samples activated at 50% strain are provided in Figure S10, confirming that once initialized, the resistance−strain waveforms remain highly stable under repeated cycling. Their normalized resistance response curves have the same shapes, and the amplitude of the curve increases with a higher strain (Figure 5a). The devices exposed to the three activation strains mentioned above were tested under the same 10% strain, and the results are reflected as three response curves with approximate amplitudes but distinctive shapes, as given in Figure 5b. Additionally, Figure 5c shows the response curves of three devices activated by the same 50% strain but cycled at different strains, which have different amplitudes and shapes. The above verification of modulation performance means that we can customize the performance of our devices according to diverse application requirements. This tunable electromechanical behavior at the device level provides a promising pathway toward programmable and multifunctional flexible electronic systems, similar to recent MXene-based wearable platforms and biointegrated electronic skins reported in the literature.[45,46] For example, the device can be attached to an athlete's joint, and the first activation strain is employed to memorize its bending amplitude and set as the standard value. Subsequently, the response signal from the device can be used as a reference to determine whether joint bending meets the standard. If the device is transferred to the same joint of another trainee, efficient guidance for the movement can also be realized.

In the following experiments, the MXene-T device was applied to detect human activities of different amplitudes, including attaching to the knee to detect squatting action, connecting to the crotch to detect goose step, and integrating into the elastic band to detect weight-bearing training (Figure 5d−f). In the detection of motion at the first two joints, the main deformation mode of the device is bending; thus, the signal response curve composed of two peaks in one cycle is different from that obtained in the previous stretching process. Although the movements of these two parts are similar, our device can still distinguish the tiny differences between them by the peak shape of the output signal. The elastic band applied in weight-bearing training mostly experiences a stretching-releasing process, so the flexible sensor integrated into it shows a signal response similar to that in Figure 5b (after 50% activation strain). Moreover, for different amplitudes of body actions, the devices in the three application examples exhibit not only a change in signal intensity but also the clear discrimination of peak shape. In previous literature studies,[41,44,48] the amplitude of body action is identified by numerical value only, which will be interfered with by many other factors, while the appearance of personalized peak shape is beneficial for the accurate quantification of action amplitude.

Another point is that long-term wearable monitoring requires the environmental stability of flexible strain sensors. Therefore, we tested the resistance change of $Ti_3C_2T_x$ MXene devices placed in an atmospheric environment. As shown in Figure S11, three representative solvents spanning different conformational regimes were selected for comparison. The relative resistance of the MXene-W device changed by 70% after 37 days of storage, while the MXene-E and MXene-M devices revealed 63 and 50% relative resistance changes, respectively. The increased resistance is attributed to the oxidation of $Ti_3C_2T_x$ MXene under oxygen and moisture exposure as well as humidity-induced interlayer spacing variation and adsorption−desorption dynamics of water molecules, which modulate interflake contact resistance. It should be noted that these measurements were performed without encapsulation to evaluate intrinsic environmental aging behavior. Meanwhile, it is confirmed that our MXene exhibited virtually no resistance variation over a week following encapsulation with PDMS to isolate it from the external environment. Importantly, although baseline resistance increases due to environmental oxidation, this drift primarily affects the absolute resistance level rather than the structural topology established during activation. Therefore, the sensing mechanism is expected to remain operative within the working strain range. In practical wearable applications, encapsulation strategies are typically employed to mitigate environmental degradation and ensure signal reliability.

CONCLUSIONS

In conclusion, the diversity of the MXene stack's conformation and the MXene film's microstructure was realized for the first time through the differential interaction between $Ti_3C_2T_x$ nanosheets and solvent molecules. When $Ti_3C_2T_x$ nanosheets are dispersed by solvents with a higher dispersion component ratio (lower polarity and hydrogen bond component ratio), the MXene stacks more easily form high-potential energy conformations and assemble into low-bulk density films. Moreover, we infer that the introduction of mixed solvent systems can further expand the regulatory space for microstructure control.

In the MXene flexible strain sensor prepared with a nonpolar solvent, we found the unique response behavior of negative resistance-strain for the first time, which corresponds to a novel compression sensing mechanism, and the performance of such devices can be modulated by prestrain. Moreover, when identifying different action amplitudes, the signal of the MXene-nonpolar solvent device shows two characteristic changes in intensity and peak shape concurrently, enhancing the distinguishability of the action amplitude and showing great potential in the application of standardized motion training.

EXPERIMENTAL SECTION

Materials

All chemical reagents were used as received. MAX precursor phases (Ti_3AlC_2, 200 mesh) were purchased from 11 Technology Co., Ltd. (JiLin, China). Lithium fluoride (LiF, Sinopharm Chemical Reagent), hydrochloric acid (HCl, General-reagent), deionized water (DI, Millipore system), ethanol (C_2H_5OH, Shanghai Lingfeng Chemical Reagent), acetone (CH_3COCH_3, General-reagent), ethyl acetate ($CH_3COOCH_2CH_3$, Sinopharm Chemical Reagent), toluene ($C_6H_5CH_3$, Shanghai Lingfeng Chemical Reagent), *m*-xylene ($C_6H_4(CH_3)_2$, Sinopharm Chemical Reagent), *n*-hexane

https://doi.org/10.1021/acsanm.5c05888
ACS Appl. Nano Mater. 2026, 9, 5132−5143

($CH_3(CH_2)_4CH_3$, Adamas-beta), polydimethylsiloxane (PDMS, Dow Corning), mixed cellulose ester filter membrane (0.22 μm GSWP, Merck Millipore), and polytetrafluoroethylene filter membrane (0.22 μm PTFE, Ahlstrom) were used.

Synthesis of Delaminated $Ti_3C_2T_x$ MXene Dispersion

According to the method reported in the previous literature,[49] $Ti_3C_2T_x$ MXene was prepared by employing the mixture of LiF and HCl to etch the precursor Ti_3AlC_2 phase. First, 1.75 g of LiF was dissolved in HCl solution (20 mL, 9 M), and then 1 g of Ti_3AlC_2 powder was slowly added to the mixture. After reacting in an oil bath at 35 °C for 24 h, the resulting mixture was washed with deionized water and centrifuged at 6000 rpm for 8 min. This step was repeated about three times until the dispersion's pH was above ~6. Subsequently, multilayer $Ti_3C_2T_x$ MXene sediment was collected to the membrane surface by vacuum filtration, and the residual moisture was further removed by following freeze-drying. To prepare delaminated $Ti_3C_2T_x$ MXene nanosheets, 0.25 g of the above sample was dispersed in 20 mL of deionized water and sonicated in an ice bath for 1 h with a continuous argon flow. Finally, the supernatant containing delaminated $Ti_3C_2T_x$ MXene was separated after centrifugation at 3500 rpm for 15 min.

Redispersion in Various Solvents and Vacuum Filtration

With the help of UV−vis spectroscopy, the concentration of the dispersion obtained in the previous step was determined. The reference dispersion's concentration was calculated from the volume of solution, and the mass of $Ti_3C_2T_x$ MXene was separated after drying. The concentrations of other dispersions were obtained by comparison with the calibration reference solution, and they were uniformly diluted to 1 mg/mL. Many individual containers were used to hold 2 or 4 mL of diluted solution, respectively. Next, liquid nitrogen was employed to rapidly freeze the dispersion and then put into a cold dryer for 24 h to prepare the delaminated $Ti_3C_2T_x$ MXene powder. After 20 mL of polar (water, ethanol, acetone, ethyl acetate) or nonpolar (toluene, *m*-xylene, *n*-hexane) solvent was introduced, the samples were temporarily evenly dispersed in various solvent systems through ultrasonic vibration for 15 min. Finally, $Ti_3C_2T_x$ MXene nanosheets were gathered on the surface of the PTFE membrane (GSWP membrane for water dispersion) by vacuum filtration, and the films with different microstructure and interfacial bonding strength were obtained.

Fabrication of Flexible Strain Sensors Based on Solvent Regulation $Ti_3C_2T_x$ MXene Films

After the resulting film was placed in a vacuum drying oven at 30 °C for 12 h, it was cut into rectangles with a size of 25 × 5 mm. As for the elastic substrate, the basic component of PDMS was mixed with a curing agent at a mass ratio of 10:1. Then, the mixture was stirred evenly and placed in a vacuum environment to remove bubbles. A cube-shaped mold (80 × 15 × 1 mm) was used to limit the liquid mixture and was prepolymerized at 80 °C for 10 min. After the rectangular film was attached to the surface of PDMS with $Ti_3C_2T_x$ MXene facing downward, the whole structure was completely cured at 80 °C for another 60 min. The PTFE filter membrane was separated from the $Ti_3C_2T_x$ MXene conductive network by tweezers. The GSWP filter membrane was separated by immersion in acetone for 30 min, and the flexible strain sensor was finally fabricated by connecting wires.

Characterization

The concentration of the delaminated $Ti_3C_2T_x$ MXene dispersion was measured by a UV−visible spectrophotometer (PerkinElmer Lambda 950, USA). The phase and *c*-axis lattice parameters were analyzed by using a high-resolution multifunction X-ray diffractometer (D8 Discover Davinci, German). The morphologies were characterized with the support of a field emission scanning electron microscope (SU8220, Hitachi, Japan). The $Ti_3C_2T_x$ MXene nanosheets dispersed in a liquid solvent environment were packaged on a chip (Nano-VIEW Cell, Suzhou Montavista Scientific Inc.) for morphology characterization. The dynamic stretching *in situ* morphologies were obtained by a desktop scanning electron microscope (Phenom XL, Thermo Fisher Scientific). The sensing performance of flexible strain sensors was tested by employing a high-precision electronic universal testing machine (CMT6103, MTS Systems, China). The current variation of the device was monitored by a potentiostat (AUTOLAB) with a constant voltage (0.1 V) applied.

Coarse-Graining Molecular Dynamics Simulation

Parameters for Energy Estimation. The energy cost to generate a specific conformation is determined by the mechanical properties and surface adhesion of the $Ti_3C_2T_x$ MXene. For the individual $Ti_3C_2T_x$ MXene nanosheet, the out-of-plane bending stiffness and in-plane tensile stiffness can be calculated from *ab initio* density functional theory (DFT),[50] while the surface energy of $Ti_3C_2T_x$ MXene can be measured based on the measured contact angles.[51]

Instead of a single layer, the $Ti_3C_2T_x$ MXene is assembled as multilayers, which possess larger bending resistance and size than individual sheets. Assuming that the sheets are closely packed within the MXene stacks, the effective in-plane tensile stiffness can be estimated by using a shear-lag model based on a layer-by-layer configuration.[52] Considering the size of sheets, the effective tensile modulus of MXene stacks (Y_{eff}) is close to that of the single layer (Y_0) due to the sufficient interlayer interactions. Therefore, the in-plane tensile stiffness is Y_0hN, where Y_0 is the tensile modulus of a single sheet, h is the thickness, and $N = H/h$ is the number of layers within an MXene stack. For the out-plane bending stiffness of $Ti_3C_2T_x$ MXene stacks, the classical relation for bending stiffness, $D = YH^3/12(1 - \nu^3)$, is not valid for multilayer 2D materials, since the interlayer slippage is inevitable.[53] Here, $H = hN$ is the thickness of MXene stacks and ν is Poisson's ratio. To address the effect of interlayer slippage, a modified formula is proposed for the effective bending stiffness

$$D_{\text{eff}} = f(N)\frac{YH^3}{12(1-\nu^2)}$$

where $f(N)$ is a function of the number of layers. According to the measures of multilayer MoS_2, graphene, and hBN based on pressurized bubbles,[53] $f(N = 20)$ ranges from 0.1 to 0.5. Here, we choose the upper limit (0.5) to estimate the bending stiffness of the $Ti_3C_2T_x$ MXene stack. The parameters of the $Ti_3C_2T_x$ MXene nanosheet and MXene stack are listed in Table S4.

Energy Estimation. The potential energy of different conformations of $Ti_3C_2T_x$ MXene stacks can be estimated based on mechanical properties and surface adhesion. We can use the completely flat stack as the energy reference, and that is, $U = 0$. For the nearly flat stacked MXene stack, the bending and stretching deformation is negligible, and the potential energy is dominated by the surface adhesion, $U = -\Gamma \times A$, where Γ is the surface energy density and A is the surface area.

For the nearly flat with edge warped, the potential energy on the ridges is additionally accounted for, $U = -\Gamma \times A + E_w l_w w \rho_w A$, where E_w is the energy density of the warped edges, l_w is the average length of warped edges, w is the width of crease, and ρ_w is the areal number density of warped edges. It is noted that the contact area is reduced due to the warped edges.

For the semiscrolled/scrolled $Ti_3C_2T_x$ MXene, the conformation is generated by several creases by folding, and thus the energy is estimated by sum of ridge energy, $U = E_f l_f w \rho_f A$, where l_f is the average length of creases and ρ_f is the areal number density of folding creases. Since the creases are nearly parallel to the axis of the scroll, we have $l_f = L = 2$ μm.

The energy of the crumpled is considered as networks of ridges and vertex, and hence, the energy is calculated as $U = \Sigma E_r l_r w + \Sigma E_v S_v$, where E_v is the energy density of the vertex and S_v is the area of vertex. For simplification, the energy is estimated in terms of statistics from the experiments, $U = (E_r w l_r \rho_r + E_v S_v \rho_v)A$, where l_r is the average length of ridge, ρ_r is the number density of the ridge, and ρ_v is the number density of the vertex.

The energy densities for the ridge (E_r) and vertex (E_v) are considered constants once the bending and tensile stiffness are determined. We thus use the coarse-grained model[28] of $Ti_3C_2T_x$

https://doi.org/10.1021/acsanm.5c05888
ACS Appl. Nano Mater. 2026, 9, 5132−5143

MXene stacks to calculate E_r and E_v. As shown in Figure S12, a crumpled $Ti_3C_2T_x$ MXene stack is generated by applying biaxial compression. According to the energy distribution remapped onto the initial flat configuration, the energy density for the ridge and vertex is E_r = 190 and E_v = 375 eV/nm^2, respectively. Here, we assume that $E_f = E_w = E_r$. We next obtain the energy landscape of $Ti_3C_2T_x$ MXene as demonstrated in Figure 2i.

■ ASSOCIATED CONTENT

Supporting Information

The Supporting Information is available free of charge at https://pubs.acs.org/doi/10.1021/acsanm.5c05888.

Additional experimental details, materials, and methods, including photographs of experimental setup (PDF)

■ AUTHOR INFORMATION

Corresponding Authors

Yin Cheng − *State Key Laboratory of High Performance Ceramics, Shanghai Institute of Ceramics, Chinese Academy of Sciences, Shanghai 200050, China;* orcid.org/0000-0001-7647-3558; Email: chengyin@mail.sic.ac.cn

Ranran Wang − *State Key Laboratory of High Performance Ceramics, Shanghai Institute of Ceramics, Chinese Academy of Sciences, Shanghai 200050, China; School of Chemistry and Materials Science, Hangzhou Institute for Advanced Study, University of Chinese Academy of Sciences, Hangzhou 310024, China;* orcid.org/0000-0001-5097-2834; Email: wangranran@mail.sic.ac.cn

Authors

Hao Ouyang − *State Key Laboratory of High Performance Ceramics, Shanghai Institute of Ceramics, Chinese Academy of Sciences, Shanghai 200050, China; Center of Materials Science and Optoelectronics Engineering, University of Chinese Academy of Sciences, Beijing 100049, China*

Hao Tang − *State Key Laboratory of High Performance Ceramics, Shanghai Institute of Ceramics, Chinese Academy of Sciences, Shanghai 200050, China; Center of Materials Science and Optoelectronics Engineering, University of Chinese Academy of Sciences, Beijing 100049, China*

Liangjing Shi − *State Key Laboratory of High Performance Ceramics, Shanghai Institute of Ceramics, Chinese Academy of Sciences, Shanghai 200050, China*

Evgeniya Sheremet − *Tomsk Polytechnic University, Tomsk 634050, Russia;* orcid.org/0000-0003-3937-8628

Raul D. Rodriguez − *Tomsk Polytechnic University, Tomsk 634050, Russia;* orcid.org/0000-0003-4016-1469

Jing Sun − *State Key Laboratory of High Performance Ceramics, Shanghai Institute of Ceramics, Chinese Academy of Sciences, Shanghai 200050, China;* orcid.org/0000-0003-1101-1584

Complete contact information is available at: https://pubs.acs.org/10.1021/acsanm.5c05888

Author Contributions

‡H.O. and H.T. contributed equally. The manuscript was written through contributions of all authors. All authors have given approval to the final version of the manuscript.

Funding

This work was financially supported by the National Key Research and Development Program of China (Grant No. 2024YFB3814100), National Natural Science Foundation of China (52203365, 62471459, U24A200901, 62261136551 (Russian Science Foundation grant No. 23−42−00081), and 62301540), the joint Project "ActFiber-FFG/CAS: 931688/030GJHZ2025029MI" managed by Austrian Research Promotion Agency (FFG) and Chinese Academy of Sciences (CAS), Shanghai International Science and Technology Cooperation Project (23520711000) from Science and Technology Commission of Shanghai Municipality. E.S. and R.D.R. acknowledge the financial support by the Russian Science Foundation grant No. 23-42-00081.

Notes

The authors declare no competing financial interest.

■ REFERENCES

(1) Naguib, M.; et al. Two-Dimensional Nanocrystals Produced by Exfoliation of Ti3AlC2. *Adv. Mater.* **2011**, *23*, 4248−4253.

(2) Gogotsi, Y. The Future of MXenes. *Chem. Mater.* **2023**, *35*, 8767−8770.

(3) Shein, I. R.; Ivanovskii, A. L. Graphene-like titanium carbides and nitrides Tin+1Cn, Tin+1Nn (n = 1, 2, and 3) from de-intercalated MAX phases: First-principles probing of their structural, electronic properties and relative stability. *Comput. Mater. Sci.* **2012**, *65*, 104−114.

(4) Tang, H.; et al. Post-processing strategies for improving the electrical and mechanical properties of MXenes. *Chem. Eng. J.* **2021**, *425*, No. 131472.

(5) Iqbal, A.; et al. Anomalous absorption of electromagnetic waves by 2D transition metal carbonitride Ti3CNTx (MXene). *Science* **2020**, *369*, 446.

(6) Iqbal, A.; Hassan, T.; Naqvi, S. M.; Gogotsi, Y.; Koo, C. M. MXenes for multispectral electromagnetic shielding. *Nature Reviews Electrical Engineering* **2024**, *1*, 180−198.

(7) Han, M.; et al. Beyond Ti3C2Tx: MXenes for Electromagnetic Interference Shielding. *ACS Nano* **2020**, *14*, 5008−5016.

(8) Liu, A.; et al. Asymmetric Structural MXene/PBO Aerogels for High-Performance Electromagnetic Interference Shielding with Ultra-Low Reflection. *Adv. Mater.* **2025**, *37*, No. e2414085.

(9) Xia, Y.; et al. Thickness - independent capacitance of vertically aligned liquid-crystalline MXenes. *Nature* **2018**, *557*, 409.

(10) Huang, H.; Yang, W. MXene-Based Micro-Supercapacitors: Ink Rheology, Microelectrode Design and Integrated System. *ACS Nano* **2024**, *18*, 4651−4682.

(11) Lukatskaya, M. R.; et al. Ultra-high-rate pseudocapacitive energy storage in two-dimensional transition metal carbides. *Nat. Energy* **2017**, *2*, 1−12.

(12) Mashtalir, O.; et al. Intercalation and delamination of layered carbides and carbonitrides. *Nat. Commun.* **2013**, *4*, 1716.

(13) Shi, Y.; et al. Prussian Blue Analogues "Dressed" in MXene Nanosheets Tightly for High Performance Lithium-Ion Batteries. *Adv. Mater.* **2025**, *37*, No. e2416665.

(14) Naguib, M.; et al. New Two-Dimensional Niobium and Vanadium Carbides as Promising Materials for Li-Ion Batteries. *J. Am. Chem. Soc.* **2013**, *135*, 15966−15969.

(15) Ming, F.; Liang, H.; Huang, G.; Bayhan, Z.; Alshareef, H. N. MXenes for Rechargeable Batteries Beyond the Lithium-Ion. *Adv. Mater.* **2021**, *33*, No. e2004039.

(16) Wang, K.; et al. Bioinspired Interlocked Structure-Induced High Deformability for Two-Dimensional Titanium Carbide (MXene)/Natural Microcapsule-Based Flexible Pressure Sensors. *ACS Nano* **2019**, *13*, 9139−9147.

(17) Bai, J.; et al. Multifunctional Flexible Sensor Based on PU-TA@MXene Janus Architecture for Selective Direction Recognition. *Adv. Mater.* **2023**, *35*, No. e2302847.

(18) Yang, Y.; Shi, L.; Cao, Z.; Wang, R.; Sun, J. Strain Sensors with a High Sensitivity and a Wide Sensing Range Based on a Ti3C2Tx

(MXene) Nanoparticle-Nanosheet Hybrid Network. *Adv. Funct. Mater.* **2019**, *29*, No. 1807882.
(19) Zhang, Y.-Z.; et al. MXenes stretch hydrogel sensor performance to new limits. *Sci. Adv.* **2018**, *4*, No. eaat0098.
(20) Hu, Y.; et al. Self-Locomotive Soft Actuator Based on Asymmetric Microstructural Ti3C2Tx MXene Film Driven by Natural Sunlight Fluctuation. *ACS Nano* **2021**, *15*, 5294−5306.
(21) Chao, M.; et al. Wearable MXene nanocomposites-based strain sensor with tile-like stacked hierarchical microstructure for broad-range ultrasensitive sensing. *Nano Energy* **2020**, *78*, No. 105187.
(22) Sun, Z.; et al. Conducting polymer hydrogels based on supramolecular strategies for wearable sensors. *Explor. (Beijing)* **2021**, *4*, No. 20220167.
(23) Zhang, L.; et al. A 3.55-microm Ultrathin, Skin-Like Mechanoresponsive, Compliant, and Seamless Ionic Conductive Electrode for Epidermal Electrophysiological Signal Acquisition and Human-Machine Interaction. *Explor. (Beijing)* **2025**, *5*, No. 20240232.
(24) He, X.; et al. Sweat-powered, skin-adhesive multimodal sensor for long-term and real-time sweat monitoring. *BMEMat* **2024**, *3*, No. e12124.
(25) Hong, X.; et al. High-permittivity Solvents Increase MXene Stability and Stacking Order Enabling Ultraefficient Terahertz Shielding. *Adv. Sci. (Weinheim)* **2024**, *11*, No. e2305099.
(26) Cao, C.; et al. Solvent-mediated structural regulation of MXene membranes for H2 purification. *Chem. Eng. Sci.* **2025**, *308*, No. 121407.
(27) Zhang, Y.; Hu, J.; Bai, G. Reversible Stacking and Delamination-Regulation of MXene via Controlled Freezing. *Small* **2024**, *20*, No. e2311218.
(28) Wang, Y.; et al. Conformational Phase Map of Two-Dimensional Macromolecular Graphene Oxide in Solution. *Matter* **2020**, *3*, 230−245.
(29) Helal, M. I.; et al. Understanding the swelling behavior of Ti3C2Tx MXene membranes in aqueous media. *J. Mater. Chem. A* **2024**, *12*, 30729−30742.
(30) Pani, J.; Borkar, H. Covalent grafting of redox-active sites onto MXenes with spinel ACo2O4 (A = Zn, Cu) integration for tailored interfacial charge storage in high-performance supercapacitors. *J. Mater. Chem. A* **2025**, *13*, 35267−35283.
(31) Vaughn, A.; et al. Selective Calixarene-Directed Synthesis of MXene Plates, Crumpled Sheets, Spheres, and Scrolls. *Chem. Eur. J.* **2017**, *23*, 8128−8133.
(32) Zhao, D.; et al. Alkali-induced crumpling of Ti3C2Tx (MXene) to form 3D porous networks for sodium ion storage. *Chem. Commun.* **2018**, *54*, 4533−4536.
(33) Hansen, C. *Hansen Solubility Parameters: A User's Handbook*. Second ed. CRC press, 2012.
(34) Ren, C. E.; et al. Charge- and Size-Selective Ion Sieving Through Ti3C2Tx MXene Membranes. *J. Phys. Chem. Lett.* **2015**, *6*, 4026−4031.
(35) Ma, Z.; et al. Ultraflexible and Mechanically Strong Double-Layered Aramid Nanofiber-Ti3C2Tx MXene/Silver Nanowire Nanocomposite Papers for High-Performance Electromagnetic Interference Shielding. *ACS Nano* **2020**, *14*, 8368−8382.
(36) Zhao, M.-Q.; et al. Flexible MXene/Carbon Nanotube Composite Paper with High Volumetric Capacitance. *Adv. Mater.* **2015**, *27*, 339−345.
(37) Yang, Y.; Cao, Z.; Shi, L.; Wang, R.; Sun, J. Enhancing the conductivity, stability and flexibility of Ti3C2Tx MXenes by regulating etching conditions. *Appl. Surf. Sci.* **2020**, *533*, No. 147475.
(38) Ling, Z.; et al. Flexible and conductive MXene films and nanocomposites with high capacitance. *Proc. Natl. Acad. Sci. U.S.A.* **2014**, *111*, 16676−16681.
(39) Wan, Y.; et al. Ultrathin, Strong, and Highly Flexible Ti3C2Tx MXene/Bacterial Cellulose Composite Films for High-Performance Electromagnetic Interference Shielding. *ACS Nano* **2021**, *15*, 8439−8449.
(40) Cai, Y.; et al. Mixed-dimensional MXene-hydrogel heterostructures for electronic skin sensors with ultrabroad working range. *Sci. Adv.* **2020**, *6*, No. eabb5367.
(41) Wang, Y.; et al. High Linearity, Low Hysteresis Ti3C2Tx MXene/AgNW/Liquid Metal Self-Healing Strain Sensor Modulated by Dynamic Disulfide and Hydrogen Bonds. *Adv. Funct. Mater.* **2023**, *33*, No. 2301587.
(42) Pu, J.-H.; et al. Multilayer structured AgNW/WPU-MXene fiber strain sensors with ultrahigh sensitivity and a wide operating range for wearable monitoring and healthcare. *J. Mater. Chem. A* **2019**, *7*, 15913−15923.
(43) Liu, Y.; et al. Ag-thiolate interactions to enable an ultrasensitive and stretchable MXene strain sensor with high temporospatial resolution. *Nat. Commun.* **2024**, *15*, 5354.
(44) Yang, H.; et al. Wireless Ti3C2Tx MXene Strain Sensor with Ultrahigh Sensitivity and Designated Working Windows for Soft Exoskeletons. *ACS Nano* **2020**, *14*, 11860−11875.
(45) Yu, S.; et al. A hyperconformal dual-modal metaskin for well-defined and high-precision contextual interactions. *Nat. Commun.* **2025**, *16*, 10573.
(46) Huang, Z.; et al. Biomimetic Pyrolytic MXene-Based Multifunctional Films with Multi-Level Structure for Wearable Piezoresistive Devices and Bioelectronics. *Adv. Funct. Mater.* **2024**, *35*, No. 2422374.
(47) Xu, L.; et al. Quasi-Homogeneous Integrated Strain Vector Sensors for Natural Human−Machine Interaction. *Adv. Funct. Mater.* **2025**, *35*, No. 2425212.
(48) Liao, H.; Guo, X.; Wan, P.; Yu, G. Conductive MXene Nanocomposite Organohydrogel for Flexible, Healable, Low-Temperature Tolerant Strain Sensors. *Adv. Funct. Mater.* **2019**, *29*, No. 1904507.
(49) Ghidiu, M.; Lukatskaya, M. R.; Zhao, M.-Q.; Gogotsi, Y.; Barsoum, M. W. Conductive two-dimensional titanium carbide 'clay' with high volumetric capacitance. *Nature* **2014**, *516*, 78−U171.
(50) Hu, T.; Yang, J.; Li, W.; Wang, X.; Li, C. M. Quantifying the rigidity of 2D carbides (MXenes). *Phys. Chem. Chem. Phys.* **2020**, *22*, 2115−2121.
(51) Zhou, H.; et al. Study on contact angles and surface energy of MXene films. *Rsc Advances* **2021**, *11*, 5512−5520.
(52) Liu, Y.; Xie, B.; Zhang, Z.; Zheng, Q.; Xu, Z. Mechanical properties of graphene papers. *Journal of the Mechanics and Physics of Solids* **2012**, *60*, 591−605.
(53) Wang, G.; et al. Bending of Multilayer van der Waals Materials. *Phys. Rev. Lett.* **2019**, *123*, No. 116101.

https://doi.org/10.1021/acsanm.5c05888
ACS Appl. Nano Mater. 2026, 9, 5132−5143